

# Design and Evaluation of a Load Control System for Biomechanical Energy Harvesters and Energy-Removing Exoskeletons

Michael Shepertycky , Yan-Fei Liu , *Fellow, IEEE*, and Qingguo Li 

**Abstract**—Controlling the timing and magnitude of electricity production is a critical factor in reducing the metabolic cost of walking with an energy-removing exoskeleton. This article outlines a novel power electronic control system designed to apply a mechanical loading profile onto the user that extracts kinetic energy. This energy extraction assists the user's muscles, thereby providing metabolic assistance while simultaneously producing electrical power. This open-loop control system estimates the state of both the exoskeleton and the user's lower limbs and uses this estimation to identify and apply a desired knee flexion moment during the terminal swing phase. The control system was evaluated using human treadmill walking experiments and benchtop testing, which determined that the system could identify the user's stride period, ground contact timing, and the device's moment arm with high accuracy and precision. Furthermore, the system could apply the desired cable force within  $\pm 2.6$  and  $-2.3$  N and the muscle-centric knee moment profile within  $\pm 0.05$  and  $-0.04$  N·m. Through proper load control, a user would benefit from walking with an energy-removing exoskeleton, regardless of the need for portable power.

**Index Terms**—Biomedical electronics, energy harvesting, exoskeletons, force control, power electronics.

Manuscript received 17 May 2022; revised 10 August 2022; accepted 20 September 2022. Recommended by Technical Editor Q. T. E. Sun and Senior Editor H. Gao. The work of Michael Shepertycky was supported by NSERC Postgraduate Scholarship under Grant PGS D2-476225-2015. This work was supported in part by NSERC under Grant RGPIN-2020-04771 to Qingguo Li and under Grant RGPIN-2019-06635 to Yan-Fei Liu. The authors Michael Shepertycky, Yan-Fei Liu, and Qingguo Li are the assignees on the patent of an energy-harvesting technology related to the research outlined in this article (U.S. Patent 9 407 125 B2). (Corresponding authors: Michael Shepertycky; Qingguo Li.)

Michael Shepertycky and Qingguo Li are with the Department of Mechanical and Materials Engineering, Queen's University, Kingston, ON K7L 3N6, Canada (e-mail: 6mys@queensu.ca; ql3@queensu.ca).

Yan-Fei Liu is with the Department of Electrical and Computer Engineering, Queen's University, Kingston, ON K7L 3N6, Canada (e-mail: yanfei.liu@queensu.ca).

This work involved human subjects or animals in its research. Approval of all ethical and experimental procedures and protocols was granted by Queen's University General Research Ethics (TRAQ: 6006569), and performed in line with the tenets of the declaration of Helsinki.

Color versions of one or more figures in this article are available at <https://doi.org/10.1109/TMECH.2022.3214419>.

Digital Object Identifier 10.1109/TMECH.2022.3214419

## I. INTRODUCTION

RECHARGING portable electronic devices, such as global positioning system units and satellite phones, has become a simple process performed without much thought. Unfortunately, recharging these devices is more difficult when the power grid is inaccessible, such as during multiweek hiking trips. This difficulty stems largely from the need to carry the required electrical power in the form of batteries, which imposes a high metabolic (i.e., energetic) burden on the user [1], [2]. For example, each kg of battery mass carried at the waist increases the metabolic cost by 3.4 W (assuming a 75 kg user) [2]. The limited operational lifespan of portable electronic devices combined with the high metabolic demand of carrying batteries for recharging has led to the development of biomechanical energy harvesters. For such devices, the user acts as a power source, converting mechanical energy harvested from their movement into electricity [3], [4], [5].

Modern biomechanical energy harvesters produce electricity, while their users engage in daily activities [6], [7], [8], [9], [10]. For example, the suspended-load harvester developed by [8] enables its user to produce electricity while walking on level ground. This device captures the mechanical energy of a loaded backpack that oscillates relative to its frame and converts this energy into electricity using a rotary generator. Another example of a harvester that produces electricity from human walking is the knee brace harvester developed by [7]. That device also uses a rotary generator, but it harvests the relative motion of the brace's two body segments, namely the thigh and shank.

Although biomechanical energy harvesters have been designed to capture energy from a wide range of motions (e.g., heel strike [11], [12] or center of mass motion [8], [13]) and joints (e.g., the ankle [6], knee [10], [14], [15], or hip [16]), their use negatively impacts their users' performance by increasing the metabolic effort required to perform the activity [7], [8], [9]. For instance, the suspended-load [8] and knee brace [7] harvesters increased the metabolic cost of walking by 22.7% and 20.8%, respectively. Notably, the negative metabolic effect commonly observed with biomechanical energy harvesters results from electricity production and the cost associated with carrying the device. To put the energetic effects of the knee brace harvester into perspective, this 20.8% increase is equivalent to carrying a 10.9 kg battery (e.g.,  $\sim 214$  Ah, 11.1 V lithium-ion) in a backpack, as estimated using results from [2]. Because

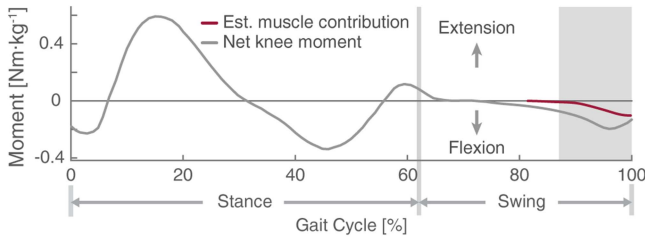


**Fig. 1.** Representative net knee moment (grey) and estimated terminal swing muscle contribution (red) profiles. Grey shading denotes the terminal swing phase. The muscle contribution was estimated using results from [21].

the device produced 4.8 W of electrical power, a user would need to walk for more than 455 h while producing electricity to see a benefit over carrying the battery (specific energy of 200 W·h/kg). These results highlight the importance of an energy harvester that minimally affects the user. If energy harvesting is detrimental to the user's performance, it might be preferable to carry batteries or to use a different device to produce the required electricity [17]. Furthermore, as battery technology continues to improve, the utility of biomechanical energy harvesters will continue to decrease.

Adverse effects of energy harvesters have been associated with the harvesting process [6], [7], [8]. Biomechanical energy harvesters apply a mechanical load onto their users, either as a force onto a body segment or a moment about a joint, to produce electricity [15], [18], [19]. Engineers and researchers have traditionally designed harvesters with constant electrical resistors (i.e., electrical loads), rather than control systems that regulate the timing and magnitude of power production. Consequently, the mechanical load that the harvester applies to the user is proportional to the angular velocity of its generator and, thereby, the motion inputted into the device [6], [7], [8], [9], [14]. Although this approach is easy to implement and has benefits in terms of electrical power production (i.e., the peak current draw is associated with the peak voltage production), this motion-dependent application of mechanical load has adverse effects on the user. For instance, devices that solely remove energy and apply the traditional motion-dependent loading profile have increased the metabolic cost of walking compared to that of normal (i.e., walking without carrying the device) and weighted walking [6], [7], [8], [9], [14]. These effects result from the mechanical loading applied by the devices inhibiting the user's motion which, in turn, causes the user to expend more energy activating their muscles to overcome the device.

Although the traditional load application disturbs the user's natural motion, Shepertycky et al. [20] demonstrated that, if properly controlled, the mechanical load resulting from power generation could assist the user's muscles in force production. Specifically, Shepertycky et al. [20] demonstrated, for the first time, that the metabolic cost of walking could be reduced by solely removing energy from the user. The device applied a moment about the user's knee that mimicked the user's muscles' contributions during the terminal swing phase of gait (Fig. 1). This muscle-centric profile was derived by subtracting

the estimated contribution of passive elements (e.g., ligaments; estimated from [21]) from the net knee moment profile. The profile reduced the metabolic cost of walking by 2.5% and reduced hamstring activity by 11.2%, compared to that of normal walking. Minimal changes in the user's kinematics and kinetics were observed, indicating that the device did not hinder the user's natural gait. This result suggests that a user would benefit from walking with this device, regardless of the need for portable power. Additionally, it demonstrates the importance of load control in increasing the utility of devices, as it enables them to assist their users while producing electricity.

Control systems capable of regulating the mechanical load applied to the user by biomechanical energy harvesters have been developed [22], [23]; however, the design and evaluation of these systems have not been reported. For example, Cervera et al. [23] developed a control system that adjusted the mechanical load applied by a knee brace harvester on a step-by-step basis to reduce the amount of metabolic energy required relative to that of weighted walking to produce electricity (i.e., the cost of harvest). Although Cervera et al. [23] reported that their control system could apply a custom loading profile, the authors never evaluated the system's load control capabilities and only examined the system while applying the traditional motion-based profile.

Another example of a harvester control system is that developed by [22]. This control system uses electromyography signals and estimates of the user's joint kinematics to apply a mechanical load proportional to the estimated knee joint moment or power. The authors evaluated the control system for its ability to estimate published knee joint moments and power from experimentally measured electromyography signals; however, they did not assess its ability to apply the desired load or its metabolic and biomechanical effects on the user [22].

This article presents the design and evaluation of a control system that regulates electrical power production, enabling the application of a programmable loading profile by an energy-removing device. The control system was evaluated using both benchtop and human walking experiments. The following section outlines the operation and mechanical design of the energy-removing exoskeleton that implemented the described control system. Section III describes the design and operation of the load control system. The methodology and results of the control system evaluation are presented in Section IV. Finally, Section V outlines conclusions and future directions for this article.

## II. DEVICE OPERATION AND MECHANICAL DESIGN

The control system described here was utilized on the energy-removing exoskeleton developed by [20]. Energy-removing exoskeletons are similar to modern energy harvesters in that they both operate by removing energy from their users and converting it into electricity; however, the primary goal of biomechanical energy harvesters is to produce a required amount of electricity, whereas the goal of energy-removing exoskeletons is to provide user assistance. The knowledge gained from developing and evaluating energy-removing exoskeletons and biomechanical energy harvesters will enable researchers to develop more

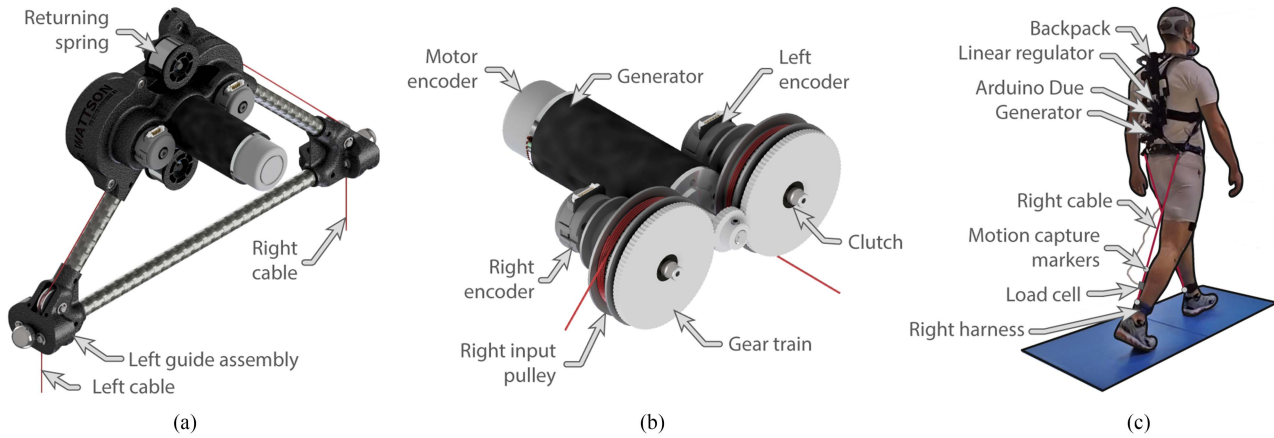


Fig. 2. Energy-removing exoskeleton. (a) Isometric view of the device. (b) View of internal components. (c) Participant walking with the exoskeleton.

metabolically efficient and useful devices. Although the control system was used to assist the hamstrings during terminal swing, it could also be used to assist other eccentrically contracting muscles during different phases of gait or activities.

The exoskeleton developed by [20] is functionally similar to the lower limb-driven energy harvester developed by [9] and [24]; however, its componentry and topology were designed to provide user assistance so as to reduce the user effort required for walking. This device was designed to assist users by reducing the amount of force that their eccentrically contracting hamstrings must produce by applying a moment about the knee during terminal swing. The exoskeleton's operation will be briefly described here for completeness before the key mechanical design features that enabled the active control of the applied load are outlined.

The fully autonomous backpack-mounted device (Fig. 2; mass: 1165 g) consists of two input cables (one per leg) that extend down from the device [Fig. 2(a) and (b)] and attach to the user's lower shanks by harnesses [Fig. 2(c)]. The other end of each cable is routed through the device by guide pulleys before being connected to its respective input pulley. As the user's knee extends forward during the swing period, the input cable is unspooled from the input pulley, driving the input shaft, gear train, and generator (EC-4 pole 305015, Maxon Motor, Switzerland). During the stance period, the roller clutches (S99NH3MURC0612, SDP/SI, USA) built into the drive gears decouple the input pulleys from the gear train, enabling the returning spring (FS0.1, Misumi, Japan) to spool the cable back onto the input pulley. Respooling the cable readies it for the subsequent swing period, while the decoupling enables the drive train and generator to be freely driven by the opposite leg during its respective swing period. This novel design takes advantage of the out-of-phase nature of the lower limbs to remove kinetic energy from both legs using a single generator.

The input cable applies a knee flexion moment because it crosses the knee joint posteriorly. This knee flexion moment ( $M_{\text{Exo}}$ ) can be calculated as the cross product of the length of the moment arm that the input cable makes with the knee ( $L_{\text{MA}}$ )

and the cable force ( $F_{\text{Cable}}$ ), assuming negligible energy loss due to the deformation of the shank harness.

$$M_{\text{Exo}} = L_{\text{MA}} \times F_{\text{Cable}}. \quad (1)$$

Similar to biomechanical energy harvesters, the force applied onto the user by the exoskeleton ( $F_{\text{Cable}}$ ) is the summation of the forces related to the device's mechanical ( $F_{\text{Mech.}}$ ) and electrical systems ( $F_{\text{Elec.}}$ )

$$F_{\text{Cable}} = F_{\text{Mech.}} + F_{\text{Elec.}}. \quad (2)$$

Complete control of the applied force would require controlling the force associated with each system. One could control the mechanical system's load by implementing mechanisms, such as continuously varying transmissions, as realized by [25] with their knee harvester. However, exoskeletons and biomechanical energy harvesters do not commonly use these control mechanisms because they are typically heavy and bulky. To reduce the weight and size of the present device, the load associated with the mechanical system was not activity-controlled; instead, its contribution was substantially reduced through design. This technique enables the electrical system to apply and control a larger portion of the desired load. Consequently, the mechanical system's contribution to the applied load primarily depends on the motion inputted into the device and the device's physical characteristics. The mechanical system's contribution is estimated as the sum of the moments related to the drive train's rotational inertia ( $M_{\text{Inertia}}$ ), friction ( $M_{\text{Friction}}$ ), and returning spring ( $M_{\text{Spring}}$ ), divided by the input pulley's radius ( $r_{\text{Input pulley}}$ )

$$F_{\text{Mech.}} = \frac{M_{\text{Inertia}} + M_{\text{Friction}} + M_{\text{Spring}}}{r_{\text{Input pulley}}}. \quad (3)$$

The most substantial reduction in the mechanical system's contribution to the applied force was achieved by reducing the gear train's reflected inertia. A gear train's reflect inertia is the sum of the rotational inertia of the device's drive components (e.g., the generator, gears, and shafts) that are translated through the gear stages [26]. The moment at the input shaft arising from the transmission's reflected inertia is the product of the gear train's reflected inertia with respect to the input shaft ( $J_{\text{Input}}$ )



and the input shaft's angular acceleration ( $\alpha_{\text{Input Shaft}}$ )

$$M_{\text{Inertia}} = \alpha_{\text{Input Shaft}} \cdot J_{\text{Input}}. \quad (4)$$

The reflected inertia of a compound gear train, commonly used in exoskeletons and biomechanical energy harvesters, with respect to its input shaft ( $J_{\text{Input}}$ ), can be calculated as

$$J_{\text{Input}} = J_1 + N_1^2 (J_2 + N_2^2 (J_3 + \dots N_n^2 (J_n + J_{\text{Machine}}))) \quad (5)$$

where  $J$  is the rotational inertia of each respective drive shaft's components (e.g., shaft, gears, or retaining rings),  $N$  is the gear ratio of the gear stage, and  $J_{\text{Machine}}$  is the rotational inertia of the machine designed to either add or remove mechanical energy, such as rotary magnetic motors and generators. These components operate most efficiently at higher rotational velocities (e.g.,  $>1000$  rpm), whereas gait is associated with slower lower limb joint velocities (e.g., knee velocities of  $\sim 20$  rpm) [4]. The fact that the performance of motors and generators is dependent on high rotational velocities has led exoskeletons and biomechanical energy harvesters to incorporate high-ratio gear trains (e.g., 1:159) [6], [7], [27], [28], even though they can apply large and uncontrollable forces due to their reflected inertia. However, reducing a gear train's reflected inertia using a direct-drive transmission is not advantageous because the rotational velocity of the generator must be high enough to produce a voltage above that of the circuit losses to control for the load applied by the electrical system. Consequently, one must balance reducing the gear train's reflected inertia and ensuring adequate voltage production. A single-stage gear train with a gear ratio of 1:3 was selected for this application to achieve this balance.

Another important factor regarding the mechanical system's contribution to the applied force and the exoskeleton's operation is the load applied by the returning spring. If the spring force cannot maintain proper cable tension, the input cable could become slack and fall off one of the guide pulleys or the input pulley itself. However, the returning spring must be just able to provide the appropriate moment about the input pulley because it applies a load onto the user throughout the entire gait cycle. Therefore, a load that is too large could hinder the user's movement. To ensure that the load applied by the spring does not hinder the user but is sufficiently able to keep the cable taut, a constant force spring with a load rating of 0.1 kgf ( $\sim 0.98$  N;  $F_{\text{Spring}}$ ) and a spring housing pulley with a radius of 0.01 m ( $r_{\text{Spring}}$ ) were utilized

$$M_{\text{Spring}} = r_{\text{Spring}} \times F_{\text{Spring}}. \quad (6)$$

Treadmill experiments revealed that the force applied by the spring could not be detected by the walker [20]. The mechanical system's contribution to the overall force was further reduced by decreasing frictional losses (i.e., by utilizing high-quality components) and increasing the user's mechanical advantage over the load (input pulley radius of 20 mm).

### III. CONTROL SYSTEM OPERATION AND DESIGN

Like biomechanical energy harvesters, the present energy-removing exoskeleton applies a mechanical load onto its user

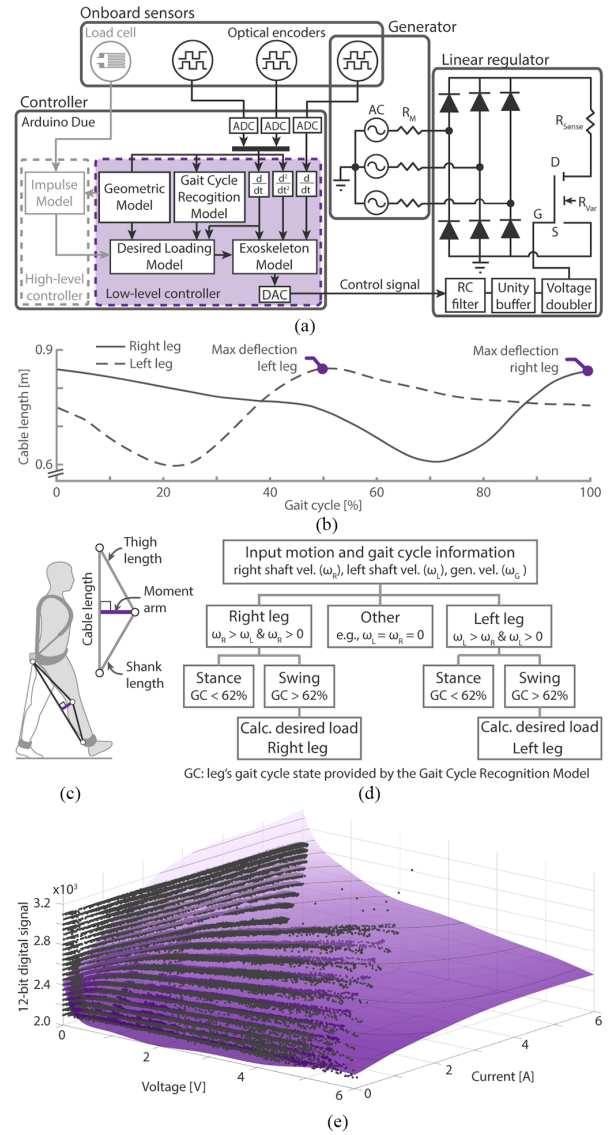


**Fig. 3.** Control system. (a) Block diagram of the control system, including the onboard sensors, generator, linear regulator, and Arduino Due. (b) Gait cycle recognition model. The time-based gait cycle recognition model detected ground contact events by identifying the maximum left and right cable lengths over a gait cycle. (c) Geometric model. The geometric model calculated the instantaneous moment arm length using the law of cosines, along with the cable length and two pseudoanthropometric measures (thigh length and shank length). (d) Force application decision tree. The desired loading model identified the swinging limb by comparing the velocities of the motor and input shafts. (e) Digital signal mapping function. The digital signal was modeled as a fifth-order polynomial (translucent purple surface), with the model-estimated current and the voltage drop over the MOSFET as independent variables. The model was developed using data (dots) collected in the benchtop model identification experiment ( $R^2 = 0.77$ ).

due to the back electromotive force (EMF) of its generator. In order to disassociate the motion-loading relationship that is commonly observed with energy harvesters [6], [8], [9], [15] so that the exoskeleton could apply a programmable loading profile, a control system was designed and implemented (Fig. 3). The standalone control system consisted of an Arduino Due microcontroller, a custom-designed linear regulator, optical encoders

(E4T-500-197-S-H-M-2, US Digital, USA), and an open-loop low-level and closed-loop high-level control scheme [Fig. 3(a)].

This article describes the open-loop low-level controller responsible for determining the state of the exoskeleton and the user's lower limbs and identifying and applying the desired knee flexion moment during the terminal swing phase. The high-level controller, described in [20], was designed for experiments that require the system to adjust the gain (i.e., magnitude) of the desired flexion moment on a step-by-step basis. For example, this high-level controller and an impulse model were used to ensure that the desired rotational average impulse applied by the exoskeleton about the user's knee was level gain planning enabled the device to take advantage of the benefits of each controller. Open-loop control was chosen for the low-level controller, primarily to decrease the control system's response time. An additional advantage of open-loop control over closed-loop control is that it requires fewer sensory components, which increases reliability and decreases weight, volume, electrical power consumption, and cost. Implementing closed-loop control for the high-level controller decreased possible systematic errors that could cause experimental discrepancies between participants and conditions that would have gone undetected and, therefore, uncorrected by an open-loop controller. The low-level controller consisted of four models: the gait cycle recognition model, the geometric model (GM), the desired loading model, and the exoskeleton model. The model parameters were identified using manufacturer-listed specifications, theoretical calculations, and benchtop testing.

### A. Gait Cycle Recognition Model

The time-based gait cycle recognition model determined the state of each of the user's legs regarding its gait cycle [i.e., % gait cycle; Fig. 3(B)]. This model segmented the motion of each leg's input cable into gait cycles by identifying ground contact events (i.e., heel strike). The model identified a ground contact event by detecting the maximum cable deflection per cycle using the optical encoders mounted on each leg's input shaft. Each leg's instantaneous state was calculated by dividing the limb's current stride time by the average stride period of the last three strides. The model used a three-stride moving average to minimize the effects of a misstep while enabling the controller to adapt rapidly to its user's changing gait. The model computed the stride period as the time between two sequential ground contact events of the same limb.

### B. Geometric Model

The GM determined the length of the moment arm made by the user's knee and the input cable [Fig. 3(c)]. This model calculated the instantaneous moment arm length ( $L_{MA}$ ) using the law of cosines, along with two pseudoanthropometric measures (thigh length:  $L_{Thigh}$  and shank length:  $L_{Shank}$ ) and the cable length ( $L_{Cable}$ )

$$L_{MA} = L_{Shank} \cdot \sin \left( a \cos \frac{L_{Shank}^2 + L_{Cable}^2 - L_{Thigh}^2}{2 \cdot L_{Shank} \cdot L_{Cable}} \right). \quad (7)$$

The pseudoanthropometric lengths were measured for each leg using a measuring tape. The shank length was measured from the cable attachment point on the harness to the femur's lateral epicondyle, and thigh length was measured from the femur's lateral epicondyle to the cable's insertion point on the device. These measurements were performed with the leg fully extended forward, mimicking the leg's posture during terminal swing (i.e., when the model is used). This model assumes that the pseudoanthropometric shank and thigh lengths are constant throughout the gait cycle, and only the cable length changes. The control system monitored the cable length using the input shaft encoders. The control system used the moment arm estimated by the GM to calculate the moment applied about the knee by the device, as described in Section II-C.

### C. Desired Loading Model

The desired loading model calculated the instantaneous input cable force required to apply the desired knee flexion moment to the swinging limb. The model first identified the swinging limb using a decision tree comparison technique [Fig. 3(d)] that compared the velocities of the input shafts and the generator and utilized gait cycle information provided by the gait cycle recognition model. Once the model identified the swinging limb, the limb's desired instantaneous knee moment was determined by evaluating the desired moment function based on the limb's current state, which was estimated by the gait cycle recognition model. An example of a desired moment function or profile is the muscle-centric profile described in [20]. The muscle-centric profile was designed to assist the user's knee flexor muscles during the terminal swing phase as a result of the device contributing a portion of the force that is naturally produced by the muscles. The desired moment profile was programmed into the microcontroller as a fifth-order polynomial function dependent on the limb's gait cycle.

The desired loading model then calculated the instantaneous desired cable force ( $F_{Desired}$ ) by dividing the instantaneous desired knee moment ( $M_{Desired}$ ) by the moment arm that the swinging limb's input cable made with its respective knee, which was estimated by the GM

$$F_{Desired} = \frac{M_{Desired}}{L_{MA}}. \quad (8)$$

### D. Exoskeleton Model

The exoskeleton model identified the 12-bit digital signal required to emulate the electrical circuit resistance in order to apply the desired cable force determined by the desired loading model. This signal was converted into an analog voltage by the Arduino Due's digital-to-analog converter before being sent to the gate of the linear regulator's metal-oxide-semiconductor field-effect transistor (MOSFET; FKI06269-ND, Sanken Electric Co., LTD., Japan).

The exoskeleton model first estimated the mechanical system's contribution to the desired cable force using (3–6) and the optical encoder measurements of the input shaft's velocity and

acceleration. The mechanical system's parameters were identified using both the manufacturer-listed specifications and theoretical calculations. For example, the bearing loads were estimated using manufacturer-listed coefficients of friction, whereas computer-aided design software was used to calculate the theoretical inertia properties of the drive components.

The exoskeleton model then calculated the electrical system's required contribution and translated it through the gear train using the following equation ( $F_{EMF}$ , i.e., EMF)

$$F_{EMF} = \frac{F_{Desired} - F_{Mech. Est.}}{N} \cdot \eta_{Mech.} \quad (9)$$

where  $F_{Mech. Est.}$  is the estimated contribution of the mechanical system,  $N$  is the gear ratio, and  $\eta_{Mech.}$  is the gear train efficiency.

The model then estimated the current draw ( $I_{Est.}$ ) required to induce the desired EMF and the resulting voltage drop across the MOSFET. The electrical current was estimated by dividing the product of the electrical system's cable force contribution and the input pulley radius ( $r_{input}$ ) by the generator's manufacturer-specified torque constant ( $K_{Torque}$ )

$$I_{Est.} = \frac{r_{input} \cdot F_{EMF}}{K_{Torque}} \quad (10)$$

The model estimated the voltage across the MOSFET ( $V_{MOS}$ ) by subtracting the estimated voltage drop due to the rectifying diodes ( $V_{Diode}$ ; SSB44-E3/52TGICT-ND, Vishay, USA), the generator's internal resistance ( $V_{Gen.}$ ), and the current-sense resistor ( $V_{sense}$ ; PF2205-0R05J1, RIEDON, USA) from the voltage produced by the generator. The voltage produced by the generator was estimated by dividing the generator's velocity ( $v_{Gen.}$ ), measured using the generator's optical encoder (225778, Maxon Motor, Switzerland), by the generator's manufacturer-specified speed constant ( $K_{Speed}$ )

$$V_{Mos} = \left( \frac{v_{Gen.}}{K_{Speed}} \right) - V_{Gen.} - (2 \cdot V_{Diode}) - V_{Sense} \quad (11)$$

The model estimated the voltage drop resulting from the generator's internal resistance by multiplying the manufacturer-specified internal resistance by the estimated current. The model calculated the voltage drop resulting from the current-sense resistor by multiplying its resistance by the estimated current. The voltage drop related to the rectification diodes was identified experimentally. Shepertycky et al. [20] previously measured the voltage and current produced across the electrical load and sense resistor, respectively.

Using a mapping function, the exoskeleton model identified the digital signal required to apply the desired mechanical load. This digital signal is converted into an analog signal by the microcontroller's digital-to-analog converter and is conditioned using a resistor–capacitor filter before reaching the MOSFET. The mapping function modeled the digital signal as a fifth-order polynomial surface [ $R^2 = 0.77$ , Fig. 3(e), translucent purple surface], with the model-estimated current and the voltage drop across the MOSFET as the two independent variables. A fifth-order polynomial surface was used because although higher degree surfaces provided a higher level of accuracy, they substantially decreased the operating speed of the microcontroller

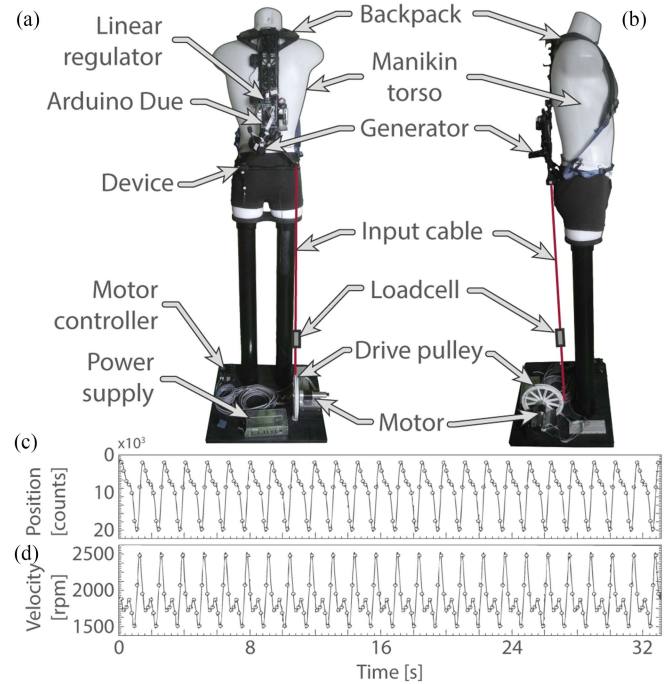


Fig. 4. Benchtop testing apparatus. (a) Front and (b) right-side views of the energy-removing exoskeleton mounted onto the benchtop testing apparatus by its backpack. (c) Position and (d) velocity profiles of the 25-step standard walking profile designed to mimic natural walking at  $1.25 \text{ m} \cdot \text{s}^{-1}$ .

(<200 Hz). The mapping function was identified using data from a benchtop model identification experiment [dots, Fig. 3(e)]. The model identification experiment consisted of 21 trials in which the benchtop testing apparatus [Fig. 4(a) and (b)] cycled the exoskeleton's right input cable through a 25-step standard walking profile [designed to mimic walking at  $1.25 \text{ m} \cdot \text{s}^{-1}$ ; Fig. 3(c) and (d)] and a 9-cycle random motion activity (performed manually). Notably, different walking speeds would result in different standard walking profiles; we selected this profile (i.e., speed) to match that used in our previous experimental protocol [20]. While the standard walking profile provided the model with information related to the average exoskeleton state, the random motion activity provided richer data regarding input cable motion. Each trial was performed using a unique constant digital signal (i.e., 21 digital signals were evaluated). The range of the 21 digital signals started at 2100 (gate voltage: 2.48 V), the experimentally determined minimum digital signal that caused a detectable change in the peak cable force, and increased to 3100 (gate voltage: 3.28 V), which was the experimentally determined maximum signal that caused a change in the peak cable force under normal walking conditions, in increments of 50 ( $\approx 0.04$  V). The order of the trials was randomized.

#### IV. CONTROL SYSTEM EVALUATION

Both benchtop and human treadmill walking experiments were conducted to examine the performance of the low-level controller including the following: 1) the gait cycle recognition model's estimation of the stride period and ground contact



timing; 2) the GM's estimation of the moment arm made by the input cable with the user's knee during the terminal swing phase; and 3) the exoskeleton model's ability to estimate the mechanical system's contribution and apply the desired cable force. The control system's ability to apply the desired knee moment was also assessed.

### A. Experimental Methodology

The performance of the gait cycle recognition model and the GM was assessed using treadmill walking experiments with six healthy males (age:  $28.8 \pm 2.8$  years, mass:  $74.4 \pm 3.4$  kg, and height:  $1.73 \pm 0.03$  m) walking at  $1.25 \text{ m} \cdot \text{s}^{-1}$  on a split-belt force-sensing treadmill (AMTI Inc., MA, USA). Before the start of the article, each participant provided written informed consent. The study protocol was approved by the Queen's University General Research Ethics Board (TRAQ: 6006569).

Each participant performed a single walking activity, which entailed walking with the exoskeleton under a light electrical load condition (12-bit digital signal set to the minimum gait threshold: 2100) for 10 min. Data to validate both models were collected during the last 2 min of the trial. Gait cycles were excluded if both of the participant's feet were simultaneously on the same force plate at the time of ground contact. The first 10 consecutive gait cycles that met the inclusion criterion and occurred within the analysis window (8–10 min) were analyzed. Control system data for validating both models were collected and processed using the onboard microcontroller at a sampling frequency above 400 Hz and logged onto a micro secure digital card (RB-Wav-16, Robotshop, Canada). Because the microcontroller operated at a variable loop speed, the instantaneous sample frequency was measured and recorded.

To validate the gait cycle recognition model, the right leg's stride period and ground contact timing detected using the model were compared to those identified using ground reaction force (GRF) measurements. The GRFs were measured using an AMTI Force-Sensing Tandem Treadmill (AMTI Inc., USA), a USB-2533 data acquisition system (Qualisys, Sweden), and Qualisys Track Manager software (Qualisys, Sweden), at a sampling frequency of 1000 Hz. The GRFs were postprocessed using a low-pass fourth-order zero-phase-shift Butterworth filter with a cutoff frequency of 20 Hz. The GRF method detected ground contact events using a vertical GRF threshold of 5 N. The two data acquisition systems (i.e., the Qualisys system and microcontroller) were synchronized using a 5 V sync pulse sent from the microcontroller to both systems. The pulse was sent to the Qualisys DAQ system using a wireless analog adaptor (Trigno Adaptor, DELSYS, USA).

The GM's ability to estimate the moment arm made by the input cable with the user's knee during the terminal swing phase was validated by comparing the moment arm length estimated by the GM to that determined using a motion capture (MC) system (Oqus, Qualisys, Sweden). The terminal swing phase was selected for analysis because the exoskeleton applied the desired knee flexion moment during this period. The moment arm determined using the MC system was calculated as the magnitude of the perpendicular vector between the knee joint

center and the cable vector [9], [20]. The knee joint center was estimated as the midpoint of the right knee's medial and lateral femoral epicondyle markers, and the cable vector was determined using two reflective markers located on the right input cable. The motion of the markers was tracked using a seven-camera reflective marker-based MC system with a sampling rate of 200 Hz. Marker data were low-pass filtered at 12 Hz using a fourth-order zero-phase-shift Butterworth filter. In order to align the moment arm profiles estimated by the GM and the MC method with respect to time (the two systems collected at different sample frequencies), the instantaneous profiles were interpolated and downsampled to 100 Hz using a cubic spline interpolation technique. The two moment arm profiles were then segmented into gait cycles using the ground contact timing estimated using the GRFs.

The exoskeleton model was validated using benchtop experiments consisting of seven trials. These trials were conducted independently from the model identification trials described in Section III-D. Five of the seven validation trials were performed with the desired cable force set to a constant load (i.e., 5, 10, 15, 20, and 25 N). The sixth validation trial was performed by sinusoidally oscillating the desired cable load between 5 and 25 N at a slightly slower frequency than that of the 25-step standard walking profile (profile: 0.87 Hz, Digital signal: 0.82 Hz). This sinusoidal desired load profile enabled the evaluation of the control system in a dynamically changing setting in which the device's operating range is tested at each point of the swing phase (i.e., when the device is engaged). The seventh trial was performed with the generator physically disconnected from the electrical circuit (i.e., open-circuit) and was used to evaluate the model's ability to estimate the mechanical system's contribution to the cable force. All seven validation trials involved the right input cable being cycled through the 25-step standard walking profile by the simulator. The order of the seven trials was randomized.

During the constant and sinusoidally oscillated desired force trials, the cable force data were segmented into periods of active control. An active control period was defined as a portion of time during which the desired cable force was less than the device's maximum force application capability and above the mechanical system's contribution. The maximum force application capability of the device was identified using the maximum constant digital signal trial of the model identification trial (i.e., 3100) and modeled as a fourth-order polynomial dependent on generator velocity. The maximum possible instantaneous cable force for each trial (excluding the open-circuit trial) was identified using the trial's measured generator velocity and the maximum cable force model. Data that were outside the active control region were not included in the statistical analysis because it would have been misleading with respect to the device's force control capabilities.

A second treadmill walking experiment involving five healthy male adults (age:  $29.2 \pm 2.7$  years, mass:  $79.6 \pm 1.4$  kg, and height:  $1.80 \pm 0.03$  m) walking at  $1.25 \text{ m/s}$  on a split-belt force-sensing treadmill was conducted to examine the control system's ability to apply a desired knee moment profile. Each participant provided written informed consent before the start

of the study (TRAQ: 6006569). Each participant performed a single 10-min walking activity that entailed walking with the exoskeleton applying the muscle-centric loading profile. Data collection, segmentation, and analysis were performed as described above. The first five consecutive gait cycles that met the inclusion criterion and occurred within the last 2 min of the trial were analyzed. The moment applied by the energy-removing exoskeleton about the user's knee was calculated using inverse dynamics [9], [20].

## B. Statistics

The Bland–Altman method was used to examine the agreement between the following parameters: 1) the gait cycle recognition model's and the GRF method's estimation of the stride period and the instance of ground contact; 2) the moment arm lengths estimated by the GM and the MC system method during the terminal swing phase; 3) the exoskeleton model's estimation and the measured mechanical system's contribution to the cable force (open-circuit condition); 4) the desired and measured cable force during the sinusoidal evaluation; and 5) the desired and applied knee moment during the treadmill walking experiment. For the validation of the gait cycle recognition and GMs, the assumption of normality for the differences between the two methods was evaluated using the Shapiro–Wilk (SW) test. If the differences were not normally distributed, a logarithmic transformation of the original data was performed and reported [29]. A test for normality was not conducted on the exoskeleton model validation samples because, based on the central limit theorem for datasets with large sample sizes ( $>30$ ), tests of normality such as the SW or Kolmogorov–Smirnov are rendered meaningless because the sampling distribution approximates a normal distribution [30]. All statistical analyses were performed using SPSS (V27, IBM Corp., USA) with the criterion for significance set at  $\alpha = 0.05$ .

## C. Limits of Agreement

The acceptable limits of agreement (LoA) between the model variables and their measured counterparts were identified a priori. Based on the authors' previous experience developing and evaluating the lower limb driven energy harvester [9], it was determined that  $\pm 2.5\%$  was an acceptable uncertainty for the stride period. Accepting a  $\pm 2.5\%$  uncertainty in the gait cycle recognition model's estimation of stride period and assuming a minimum step period of 1 s (estimated from preliminary trials), the acceptable LoA between the two measurements would be approximately  $\pm 0.025$  s. The  $\pm 2.5\%$  uncertainty ( $\delta P$ ) in the stride period would result from the uncertainty propagated by detecting two ground contact events. Because two sequential ground contact events would have the same uncertainty in their detection ( $\delta t_1 = \delta t_2$ ), the acceptable LoA between the two measures' estimates of ground contact timing would be approximately  $\pm 0.018$  s

$$\delta P = \sqrt{(\delta t_1)^2 + (\delta t_2)^2}. \quad (12)$$

The design criterion established during the development of the exoskeleton specified that the uncertainty of the knee flexion moment applied by the device was to be within  $\pm 10\%$  of the maximum applied moment of  $3.6 \text{ N}\cdot\text{m}$  (i.e.,  $\pm 0.36 \text{ N}\cdot\text{m}$ ). Applying this design criterion and allowing the uncertainty to propagate equally from the moment arm length estimation and the applied cable force, the moment arm and cable force's maximum acceptable uncertainty was  $\pm 7.1\%$  (13). Assuming the shortest moment arm length of  $0.12 \text{ m}$  (identified through preliminary trials), the acceptable LoA for the two techniques' estimations of the moment arm would be  $\pm 0.0085 \text{ m}$  ( $8.5 \text{ mm}$ ). The shortest estimated moment arm length was selected because it would lead to the narrowest acceptable LoA

$$\frac{\delta M_{\text{Applied}}}{|M_{\text{Applied}}|} = \sqrt{\left(\frac{\delta L_{\text{MA}}}{L_{\text{MA}}}\right)^2 + \left(\frac{\delta F_{\text{Cable}}}{F_{\text{Cable}}}\right)^2}. \quad (13)$$

Assuming a maximum cable force applied by the exoskeleton of  $30 \text{ N}$  and an acceptable cable force uncertainty of  $\pm 7.1\%$  of the maximum applied load, the LoA of the desired and measured cable force is  $\pm 2.13 \text{ N}$ . Based on previous experience and preliminary data, the cable force uncertainty was allowed to propagate disproportionately from the mechanical and electrical systems. As a result, the acceptable uncertainty of the mechanical system's contribution was deemed to be  $\pm 1.00 \text{ N}$ , whereas the acceptable uncertainty of the electrical system's contribution was  $\pm 1.88 \text{ N}$ . This unequal allocation of uncertainty was acceptable because controlling the force related to the electrical system was expected to be more challenging than predicting the mechanical system's contribution.

## D. Results and Discussion

1) *Gait Cycle Recognition Model*: The stride periods estimated using the gait cycle recognition model and the GRF method [Fig. 5(a)] did not differ significantly [mean difference:  $-0.0001 \pm 0.0009 \text{ s}$ , two-tailed, one-sample t-test:  $t_{(59)} = -0.139$ ,  $p = 0.890$ ; SW test:  $W_{(60)} = 0.966$ ,  $p = 0.088$ , Fig. 5(b)]. There was also no significant proportional bias between the two measures of the stride period ( $t_{(58)} = -0.293$ ,  $p = 0.770$ , slope:  $-0.007$ , intercept:  $0.008$ ). Furthermore, the LoAs of the two measures (upper:  $0.014 \text{ s}$  and lower:  $-0.015 \text{ s}$ ) were also within the acceptable range. The instance of ground contact estimated using the gait cycle recognition model and the GRF method [Fig. 5(a)] did not significantly differ [mean difference:  $-0.0012 \pm 0.0010 \text{ s}$ ,  $t_{(59)} = -1.164$ ,  $p = 0.249$ ;  $W_{(60)} = 0.969$ ,  $p = 0.124$ , Fig. 5(c)]. There was also no significant proportional bias between the two measures ( $t_{(58)} = -0.979$ ,  $p = 0.332$ , slope:  $-0.0003$ , intercept:  $0.0007$ ), and their LoAs (upper:  $0.0140 \text{ s}$  and lower:  $-0.0164 \text{ s}$ ) were within the acceptable range. These results indicate that the gait cycle recognition model could identify a gait cycle within an acceptable range of uncertainty and was thus deemed sufficient.

2) *Geometric Model*: Fig. 6(a) illustrates the moment arm lengths that were estimated using the GM and the MC method as a function of the percent of the gait cycle. Although large deviations between the two techniques can be observed during the stance period, the two techniques were not significantly



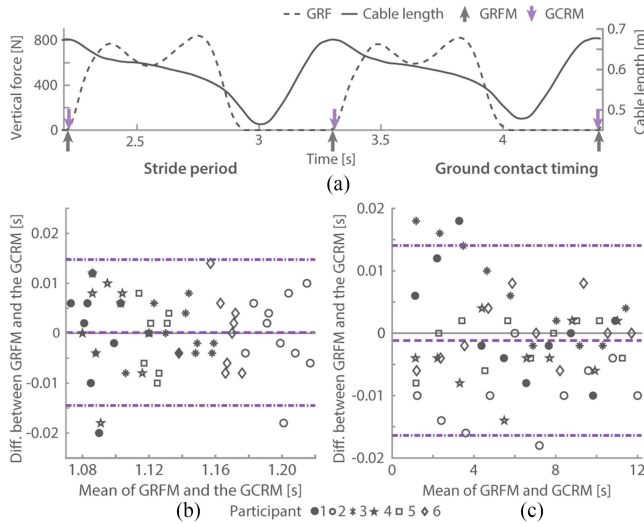


**Fig. 5.** Ground contact and stride period recognition. (a) Vertical ground reaction forces (GRFs; dashed grey line, left vertical axis) and the right leg's cable length (solid grey line, right vertical axis) over two consecutive steps of a representative participant. Arrows indicate ground contact events identified by the ground reaction force method (GRFM: grey) and the gait cycle recognition model (GCRM: purple). (b) Bland–Altman plot comparing the GRFM and GCRM estimates of the stride period for six participants (dashed purple line: mean difference, dash-dot lines: upper and lower 95% limits of agreement). (c) Bland–Altman plot comparing the GRFM and GCRM estimates of ground contact timing for six participants.

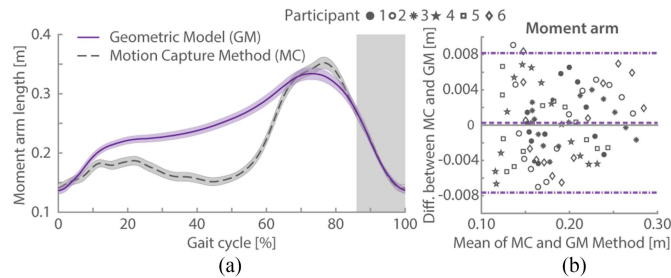


**Fig. 6.** Moment arm lengths estimated by the geometric model (GM) and the motion capture method (MC). (a) Cross-subject average moment arm length estimated by the GM (purple) and by the MC (grey) (means  $\pm$  standard error of the mean). Grey shading denotes the terminal swing phase. (b) Bland–Altman plot comparing the GM and MC estimates of moment arm length during terminal swing (dashed purple line: mean difference, dash-dot lines: upper and lower 95% limits of agreement).

different during the terminal swing phase [mean difference:  $-0.0003 \pm 0.0004$  m, two-tailed, one-sample  $t$ -test:  $t_{(82)} = 0.594$ ,  $p = 0.554$ ; SW test:  $W_{(83)} = 0.974$ ,  $p = 0.085$ ; Fig. 6(b)]. There was also no significant proportional bias between the two measures ( $t_{(81)} = 1.231$ ,  $p = 0.222$ ; slope: 0.0013, intercept:  $-0.002$ ). Furthermore, the LoAs of the two measures (upper: 0.0082 m and lower:  $-0.0076$  m) were within the acceptable range. The discrepancy observed between the GM and MC during the stance period most likely resulted from the cable length being governed during this period primarily by the overall limb motion (i.e., moving from a leading to a trailing position), rather than the knee joint motion, as assumed by the GM. The

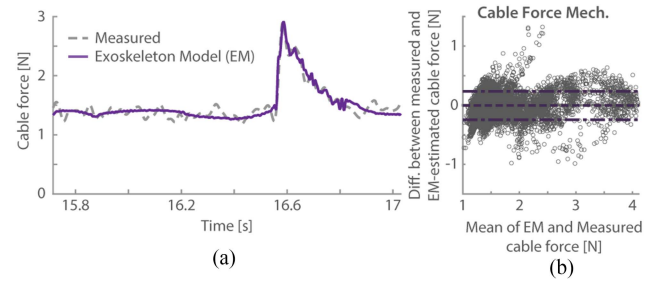


**Fig. 7.** Exoskeleton model's (EM) prediction of the open-circuit cable force. (a) Representative open-circuit cable force estimated by the EM (solid purple) and measured using an in-series load cell (dashed grey) during a single step from the 25-step standard walking profile trial. (b) Bland–Altman plot comparing the measured and EM-estimated cable forces (dashed purple: mean difference, dash-dot purple: upper and lower 95% limits of agreement).

overall limb motion being the primary factor in the input cable length during the stance phase is due to the device being located posterior to the hip and not at the hip center.

**3) Exoskeleton Model:** Fig. 7(a) illustrates a representative profile of the measured and model-predicted open-circuit cable forces. This representative waveform demonstrates that the exoskeleton model accurately estimated the cable force related to the mechanical system throughout the simulated gait cycle. Although the measured and model-predicted open-circuit cable forces were significantly different and had a significant proportional bias, the mean difference and the slope of the bias were within the load cell's measurement uncertainty [mean difference:  $-0.005 \pm 0.001$  N, one-sample, two-tailed  $t$ -test:  $t_{(26927)} = -6.130$ ,  $p < 0.001$ ; proportional bias:  $t_{(26926)} = 24.379$ ,  $p < 0.001$ , slope: 0.047, intercept: 0.074; Fig. 7(b)]. The upper and lower LoAs of the two measures were 0.236 and  $-0.245$  N, respectively. Because the mean difference and the proportional bias were outside the measurement system's resolution and the LoAs were well within the acceptable range, the exoskeleton model's capability of estimating the mechanical system's contribution to the cable force was deemed adequate for the present application.

Fig. 8(a)–(d) illustrates representative profiles of the applied (purple) and desired (dash-dot grey) cable forces during the sinusoidal force validation trials. The desired and applied cable forces were found to be significantly different, with the device applying a force lower than the desired force [mean difference:  $0.150 \pm 0.028$  N, two-tailed, one-sample  $t$ -test:  $t_{(2072)} = 5.428$ ,  $p < 0.001$ ; Fig. 8(e)]. There was no significant proportional bias between the desired and applied cable forces ( $t_{(2071)} < 1.71$ ,  $p = 0.118$ , slope: 0.007, intercept: 0.066); however, the LoAs were found to be slightly outside the acceptable range of  $\pm 2.13$  N (upper: 2.614 N and lower:  $-2.314$  N).

Although the exoskeleton applied the desired cable force reasonably well across the active control region, it struggled to achieve the desired load as it neared its maximum force capabilities (dashed grey); this was also apparent in the constant desired force trials [Fig. 8(f)]. These periods during which the exoskeleton struggled to achieve the desired load were also

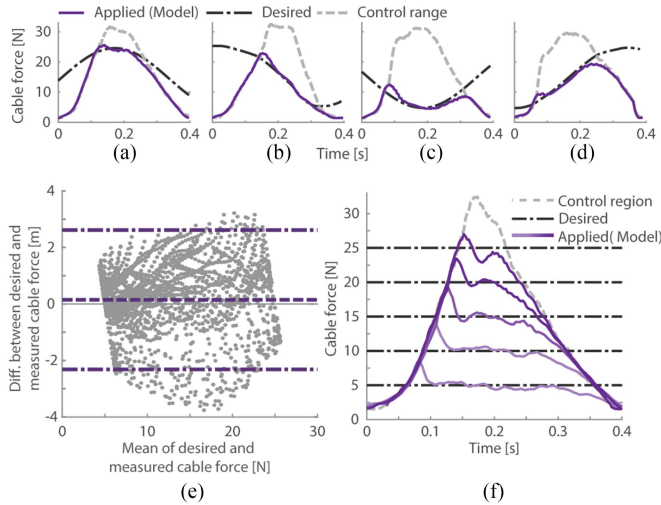


**Fig. 8.** Force control capabilities of the exoskeleton during force validation trials. Representative waveforms of the sinusoidal force validation trials in which the exoskeleton (purple; measured) attempted to apply a sinusoidal desired loading profile (solid grey) over the swing phase of the standard walking profile. The desired cable force is shown for the peak (a), descent (b), trough (c), and rise (d) of the sinusoidal function. The dashed grey line represents the maximum instantaneous cable force that the exoskeleton can apply. (e) Bland–Altman plot comparing the exoskeleton's force application to the desired cable force (dashed purple line: mean difference, dash-dot lines: upper and lower 95% limits of agreement). (f) Representative waveforms from the constant force validation trials in which the exoskeleton attempted to apply a constant 5, 10, 15, 20, or 25 N cable force over the swing phase of the standard walking profile.

associated with low-voltage production. This limitation may be partially due to the mapping function's inaccuracy in identifying the required digital signal within the region of low voltage [ $\leq 0.5$  V, Fig. 3(e)]. Small errors in the model-predicted voltage ( $\pm 0.05$  V) within this low-voltage region relate to large changes in the predicted digital signal ( $\pm 70$ ). Therefore, both modeling and measurement errors greatly affect the device's ability to apply the desired load in this region. This discrepancy between the desired and applied cable forces during periods of low-voltage highlights the importance of maintaining the balance between voltage production and reducing the load related to the mechanical system.

**4) Overall Moment Application:** Fig. 9(a) illustrates a representative profile of the applied (purple) and desired (dash-dot grey; muscle-centric profile) knee moment during a single step. There was no significant difference between the desired and applied knee moments [mean difference:  $0.001 \pm 0.001$  N·m, two-tailed, one-sample t-test:  $t_{(1093)} = 1.782$ ,  $p = 0.075$ ; Fig. 9(b)]. Additionally, there was no significant proportional bias between the desired and applied moments ( $t_{(1092)} < 1.400$ ,  $p = 0.162$ , slope:  $-0.004$ , intercept:  $0.003$ ). The LoAs were well within the acceptable range of  $\pm 0.36$  N·m (upper:  $0.04$  N·m and lower:  $-0.04$  N·m). This result is due to the muscle-centric profile being within the device's ability to apply force and estimate the moment arm.

The theoretical uncertainty in the applied moment can be estimated by propagating the uncertainty in the low-level controller's force application (upper:  $2.614$  N and lower:  $-2.314$

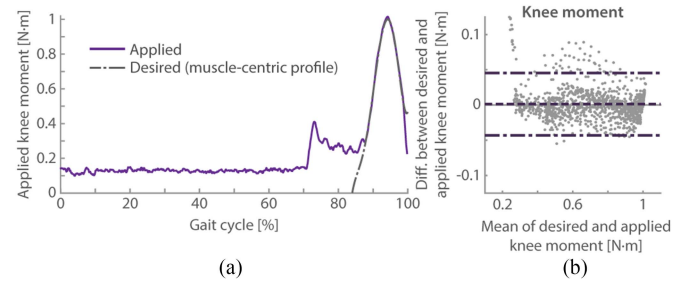


**Fig. 9.** Moment control capabilities of the exoskeleton while applying the muscle-centric profile. (a) Representative applied (purple) and desired (dash-dot grey) knee moment during a single step. (b) Bland–Altman plot comparing the desired and applied knee moment (dashed purple: mean difference, dash-dot purple: upper and lower 95% limits of agreement).

N; assuming a max theoretically applied force of  $30$  N) and moment arm estimation (upper:  $0.0082$  m and lower:  $-0.0076$  m; assuming a theoretical moment arm of  $0.12$  m) using (13). This would result in a theoretical uncertainty in the applied moment between  $0.36$  N·m ( $11.1\%$  of maximum load at terminal swing) and  $-0.32$  N·m ( $-10.0\%$  of maximum load at terminal swing), assuming a maximum moment of  $3.6$  N·m.

Given the control system's high degree of accuracy with respect to mechanical load application, the exoskeleton was deemed acceptable for removing energy during the terminal swing phase of gait. However, caution should be exercised when designing the desired loading profiles to ensure that the desired moment was well within the device's maximum load capabilities whenever possible.

## V. CONCLUSION

Actively controlling energy extraction has been identified as a critical factor in enabling energy-removing exoskeletons and biomechanical energy harvesters to generate electrical power while also reducing the metabolic cost of walking [20]. The need for active control results from the control system being able to apply the mechanical load onto the user in such a way as to reduce the amount of force the muscles must produce. However, without actively controlling this mechanical load, energy-removing exoskeletons and energy harvesters could apply loads that impede their users' natural motion. In this article, a power electronic control system is described that is capable of regulating the electrical current and estimating the voltage production through a linear regulator to reduce the effort of walking while simultaneously producing electrical power. The present benchtop and human walking experiments demonstrated the control system's high level of accuracy in terms of mechanical load application as well as its ability to identify human parameters.

Future biomechanical energy harvesting control systems should focus on implementing a "human-in-the-loop" approach for identifying user-specific assistance profiles [31], [32]. This approach automates the profile identification process by tuning the loading profile based on real-time physiological measurements. This approach, combined with a force control system

like the one described here, would enable the device to sense and adapt to the user's continuously changing gait [33].

### ACKNOWLEDGMENT

The authors thank K. Deluzio for supplying equipment in the Queen's HMRL and C. Soutar for providing editorial feedback.

### REFERENCES

- [1] R. G. Soule and R. F. Goldman, "Energy cost of loads carried on the head, hands, or feet," *J. Appl. Physiol.*, vol. 27, no. 5, pp. 687–690, 1969, doi: [10.1152/jappl.1969.27.5.687](#).
- [2] R. C. Browning, J. R. Modica, R. Kram, and A. Goswami, "The effects of adding mass to the legs on the energetics and biomechanics of walking," *Med. Sci. Sports Exercise*, vol. 39, no. 3, pp. 515–525, 2007, doi: [10.1249/mss.0b013e31802b3562](#).
- [3] Y. Liu et al., "Piezoelectric energy harvesting for self-powered wearable upper limb applications," *Nano Select*, vol. 2, no. 8, pp. 1459–1479, 2021, doi: [10.1002/nano.202000242](#).
- [4] R. Riemer and A. Shapiro, "Biomechanical energy harvesting from human motion: Theory, state of the art, design guidelines, and future directions," *J. NeuroEng. Rehabil.*, vol. 8, no. 1, pp. 1–13, 2011.
- [5] A. Delnavaz and J. Voix, "Flexible piezoelectric energy harvesting from jaw movements," *Smart Mater. Struct.*, vol. 23, no. 10, 2014, Art. no. 105020, doi: [10.1088/0964-1726/23/10/105020](#).
- [6] M. Cai, W. Liao, and J. Cao, "A smart harvester for capturing energy from human ankle dorsiflexion with reduced user effort," *Smart Mater. Struct.*, vol. 28, no. 1, 2018, Art. no. 015026, doi: [10.1088/1361-665X/aaed66](#).
- [7] J. M. Donelan, Q. Li, V. Naing, J. A. Hoffer, D. J. Weber, and A. D. Kuo, "Biomechanical energy harvesting: Generating electricity during walking with minimal user effort," *Science*, vol. 319, pp. 807–811, 2008, doi: [10.1126/science.1149860](#).
- [8] L. C. Rome, L. Flynn, E. M. Goldman, and T. D. Yoo, "Generating electricity while walking with loads," *Science*, vol. 309, pp. 1725–1729, 2005, doi: [10.1126/science.1111063](#).
- [9] M. Shepertycky and Q. Li, "Generating electricity during walking with a lower limb-driven energy harvester: Targeting a minimum user effort," *Plos One*, vol. 10, no. 6, 2015, Art. no. e0127635, doi: [10.1371/journal.pone.0127635](#).
- [10] F. Gao, G. Liu, B. L.-H. Chung, H. H.-T. Chan, and W.-H. Liao, "Macro fiber composite-based energy harvester for human knee," *Appl. Phys. Lett.*, vol. 115, no. 3, 2019, Art. no. 033901, doi: [10.1063/1.5098962](#).
- [11] N. S. Shenck and J. A. Paradiso, "Energy scavenging with shoe-mounted piezoelectrics," *IEEE Micro*, vol. 21, no. 3, pp. 30–42, May/Jun. 2001, doi: [10.1109/40.928763](#).
- [12] H. Xia and P. B. Shull, "Preliminary testing of an angled sliding shoe for potential human energy harvesting applications," in *Proc. IEEE 2nd Int. Conf. Robot. Automat. Sci.*, 2018, pp. 147–150, doi: [10.1109/ICRAS.2018.8442419](#).
- [13] J. Feenstra, J. Granstrom, and H. Sodano, "Energy harvesting through a backpack employing a mechanically amplified piezoelectric stack," *Mech. Syst. Signal Process.*, vol. 22, no. 3, pp. 721–734, 2008, doi: [10.1016/j.ymssp.2007.09.015](#).
- [14] J. Fan, C. H. Xiong, Z. K. Huang, C. B. Wang, and W. bin Chen, "A lightweight biomechanical energy harvester with high power density and low metabolic cost," *Energy Convers. Manage.*, vol. 195, pp. 641–649, 2019, doi: [10.1016/j.enconman.2019.05.025](#).
- [15] Q. Li, V. Naing, and J. M. Donelan, "Development of a biomechanical energy harvester," *J. NeuroEng. Rehabil.*, vol. 6, no. 1, pp. 22–34, 2009, doi: [10.1186/1743-0003-6-22](#).
- [16] D. Dai and J. Liu, "Hip-mounted electromagnetic generator to harvest energy from human motion," *Front. Energy*, vol. 8, no. 2, pp. 173–181, 2014, doi: [10.1007/s11708-014-0301-2](#).
- [17] E. Schertzer and R. Riemer, "Harvesting biomechanical energy or carrying batteries? An evaluation method based on a comparison of metabolic power," *J. NeuroEng. Rehabil.*, vol. 12, no. 1, pp. 1–12, 2015, doi: [10.1186/s12984-015-0023-7](#).
- [18] A. J. Dickson, S. Burton, M. Shepertycky, Y.-F. Liu, and Q. Li, "Digitally controlled energy harvesting power management system," *IEEE J. Emerg. Sel. Topics Power Electron.*, vol. 4, no. 1, pp. 303–317, Mar. 2016, doi: [10.1007/1-4020-0613-6\\_11008](#).
- [19] J. P. Martin, M. Shepertycky, Y. F. Liu, and Q. Li, "Lower limb-driven energy harvester: Modeling, design, and performance evaluation," *J. Med. Devices Trans. ASME*, vol. 10, no. 4, pp. 1–9, 2016, doi: [10.1115/1.4033014](#).
- [20] M. Shepertycky, S. Burton, A. Dickson, Y.-F. Liu, and Q. Li, "Removing energy with an exoskeleton reduces the metabolic cost of walking," *Science*, vol. 372, no. 6545, pp. 957–960, 2021, doi: [10.1126/science.aba9947](#).
- [21] B. Whittington, A. Silder, B. Heiderscheit, and D. G. Thelen, "The contribution of passive-elastic mechanisms to lower extremity joint kinetics during human walking," *Gait Posture*, vol. 27, no. 4, pp. 628–634, 2008, doi: [10.1016/j.gaitpost.2007.08.005](#).
- [22] J. C. Selinger and J. M. Donelan, "Myoelectric control for adaptable biomechanical energy harvesting," *IEEE Trans. Neural Syst. Rehabil. Eng.*, vol. 24, no. 3, pp. 364–373, Mar. 2016, doi: [10.1109/TNSRE.2015.2510546](#).
- [23] A. Cervera, Z. Rubinshtein, M. Gad, R. Riemer, and M. Peretz, "Biomechanical energy harvesting system with optimal cost-of-harvesting tracking algorithm," *IEEE J. Emerg. Sel. Topics Power Electron.*, vol. 4, no. 1, pp. 293–302, Mar. 2016, doi: [10.1109/JESTPE.2015.2514079](#).
- [24] M. Y. Shepertycky, Q. Li, and Y.-F. Liu, "Biomechanical electrical power generation apparatus," U.S. Patent 9,407,125, 2013, doi: [10.1021/n10602701](#).
- [25] Y. Ikawa, T. Kobayashi, and T. Matsubara, "Biomechanical energy harvester with continuously variable transmission: Prototyping and preliminary evaluation," in *Proc. IEEE/ASME Int. Conf. Adv. Intell. Mechatron.*, 2018, pp. 1045–1050, doi: [10.1109/AIM.2018.8452395](#).
- [26] F. Roos and C. Spiegelberg, "Relations between size and gear ratio in spur and planetary gear trains (No. 1)," KTH. 2005. [Online]. Available: <https://www.diva-portal.org/smash/record.jsf?dswid=9071&pid=diva2%3A12428>
- [27] M. Shepertycky, J.-T. Zhang, Y.-F. Liu, and Q. Li, "Development of an energy harvesting backpack and performance evaluation," in *Proc. IEEE 13th Int. Conf. Rehabil. Robot.*, 2013, pp. 1–6.
- [28] J. M. Altman and D. G. Bland, "Measurement in medicine: The analysis of method comparison studies," *J. Roy. Statist. Soc.: Ser. D*, vol. 32, no. 3, pp. 307–317, 1983.
- [29] S. G. Kwak and J. H. Kim, "Central limit theorem: The cornerstone of modern statistics," *Korean J. Anesthesiol.*, vol. 70, no. 2, 2017, Art. no. 144, doi: [10.4097/kjae.2017.70.2.144](#).
- [30] R. W. Jackson and S. H. Collins, "Heuristic-based ankle exoskeleton control for co-adaptive assistance of human locomotion," *IEEE Trans. Neural Syst. Rehabil. Eng.*, vol. 27, no. 10, pp. 2059–2069, Oct. 2019, doi: [10.1109/TNSRE.2019.2936383](#).
- [31] J. Zhang et al., "Human-in-the-loop optimization of exoskeleton assistance during walking," *Science*, vol. 356, no. 6344, pp. 1280–1284, 2017.
- [32] J. R. Koller, D. H. Gates, D. P. Ferris, and C. D. Remy, "Body-in-the-loop optimization of assistive robotic devices: A validation study," *Robot.: Sci. Syst.*, vol. 2016, pp. 1–10, 2016, doi: [10.15607/rss.2016.xii.007](#).
- [33] R. W. Nuckols, K. Z. Takahashi, D. J. Farris, S. Mizrachi, R. Riemer, and G. S. Sawicki, "Mechanics and energetics of walking and running up and downhill: A joint-level perspective to guide design of lower-limb exoskeletons," *PLoS One*, vol. 15, no. 8, 2020, Art. no. e0231996, doi: [10.1101/2020.04.07.029579](#).

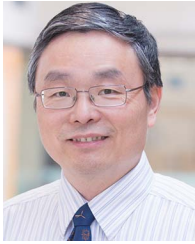


**Michael Shepertycky** received the Ph.D. degree in mechanical engineering with a specialty in biomedical engineering from the Department of Mechanical and Materials Engineering, Queen's University, Kingston, ON, Canada, in 2021.

His work on an energy-removing lower limb exoskeleton has been featured in the journal *Science*. His research interests include biomechanical energy harvesting, wearable robotics, and the biomechanics and energetics of human gait.

Dr. Shepertycky as the recipient of the 2021 Queen's University Engineering and Applied Science Outstanding Thesis Award for the Ph.D. thesis, entitled "Development and Evaluation of an Energy-Removing Lower-Limb Exoskeleton for Human Gait Assistance."

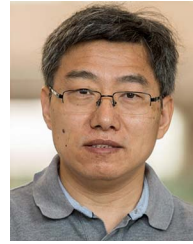




**Yan-Fei Liu** (Fellow, IEEE) received the bachelor's and master's degrees in electrical engineering from the Department of Electrical Engineering, Zhejiang University, Hangzhou, China, in 1984 and 1987, respectively, and the Ph.D. degree in electrical engineering from the Department of Electrical and Computer Engineering, Queen's University, Kingston, ON, Canada, in 1994.

He was a Technical Advisor with the Advanced Power System Division, Nortel Networks, Ottawa, Canada, from 1994 to 1999. Since 1999, he has been with the Queen's University, where he is currently a Professor with the Department of Electrical and Computer Engineering. He has authored around 270 technical papers in IEEE Transactions and conferences and holds 53 U.S. patents. He has written a book titled "High Frequency MOSFET Gate Drivers: Technologies and Applications," published by IET. He is also a Principal Contributor for two IEEE standards. His research interests include optimal application of GaN and SiC devices to achieve small-size and high-efficiency power conversion, 99% efficiency power conversion with extremely high power density, digital control technologies for high efficiency, fast dynamic response dc-dc switching converter and ac-dc converter with power factor correction, resonant converters, and server power supplies, and LED drivers.

Dr. Liu was the recipient of the "Prize of Excellence in Research" at Queen's University in 2020 and the "Modeling and Control Achievement Award" from the IEEE Power Electronics Society in 2017. He was the Vice President of Technical Operations of IEEE PELS from 2017 to 2020. He has been serving as an Editor of IEEE JOURNAL OF EMERGING AND SELECTED TOPICS OF POWER ELECTRONICS, since 2013. He was the General Chair of ECCE 2019, which was held in Baltimore, MD, USA, in 2019.



**Qingguo Li** received the Ph.D. degree in engineering science from the School of Engineering, Simon Fraser University, Burnaby, BC, Canada, in 2006.

In 2009, he joined the Queen's University, Kingston, ON, Canada, where he is currently an Associate Professor with the Department of Mechanical and Materials Engineering. His work on energy harvesters and exoskeletons has been featured in a peer-reviewed article in the journal *Science*. His research interests include energy harvesting, wearable robotics, and wearable sensors for human movement analysis.

Dr. Li was a recipient of the Governor General's Gold Medal in 2006.